2.5-Dimensional Electrical Resistivity Tomography for Cylindrical Objects Incorporating the Modified Optimization Wavenumbers

Lan Gao[1,2], Xiaodong Yang[1,2,3], Hongwei Zhou[4], Mingxin Yue[1,2,3], Bowen Chen[1,2], Daiming Hu[1,2], Xiaoping Wu[1,2,3*]

[1] Univ Sci & Technol China, Sch Earth & Space Sci, Hefei 230026, Peoples R China

[2] CAS Ctr Excellence Comparat Planetol, Hefei 230026, Peoples R China

[3] Univ Sci & Technol China, Mengcheng Natl Geophys Observ, Hefei 230026, Peoples R China

[4] Hubei Key Laboratory of Earthquake Early Warning, Institute of Seismology, CEA, Wuhan Institute of Earthquake Engineering Co. Ltd. 40 Hongshance Road, Wuhan, China, 430071.

Corresponding author: Xiaoping Wu (wxp@ustc.edu.cn.)

Key Points:

- We present a 2.5-dimensional ERT scheme for cylindrical objects incorporating the modified optimization wavenumbers.
- The modified optimization wavenumber selection based on the analytic solution of an infinitely long homogeneous cylinder is firstly analyzed.
- Both numerical analysis and laboratory experiments prove that the modified optimization wavenumbers can achieve higher computing accuracy.

Abstract

More and more applications of electrical resistivity tomography (ERT) for cylindrical objects have been rising in recent decades. This paper presents a 2.5-dimensional differential resistivity reconstruction scheme of cylindrical objects. The forward modeling algorithm incorporates the modified optimization wavenumbers to achieve an accurate 2.5-dimensional forward modeling. The modified optimization wavenumber selection is based on the approximate analytic solution of the circumference potential distribution of an infinitely long homogeneous cylindrical model, making it more accurate for cylindrical objects compared to the traditional optimization wavenumber selection which is only applicable for the half-space condition. In the laboratory, we measured the resistivity and resistance distributions of the sodium chloride solution-filled cylindrical tanks with/without a high resistivity rubber bar in the central. The modified and traditional optimization wavenumbers are included respectively to calculate the resistance distribution of the measured objects. The comparison results between the calculated and measured resistance distribution show that the modified optimization wavenumbers proposed in this paper can obtain higher calculation accuracy. The differential ERT incorporating the modified optimization wavenumbers is then employed to reconstruct the resistivity distribution of the cylindrical objects. The inversed resistivity values are in good agreement with the measured values. We, therefore, conclude that the modified optimization wavenumbers can result in better accuracy than the traditional one and the proposed 2.5-dimensional differential resistivity reconstruction scheme is time-saving and has great promise for the imaging of cylindrical objects.

Plain Language Summary

Electrical resistivity tomography as a widely used method has been extended to many new applications that focus on cylindrical objects. Here we analyze the approximate analytic solution of the circumference potential distribution of an infinitely long homogeneous cylindrical model, based on which the modified optimization wavenumber selection is derived. By incorporating the modified optimization wavenumber, we present a 2.5-dimensional differential resistivity reconstruction scheme for cylindrical objects. Both numerical analysis and laboratory experiments demonstrate that the modified optimization wavenumber can improve the accuracy of electrical resistivity modeling and, ERT, together with the modified optimization wavenumber, has great promise for detecting cylindrical objects such as tree trunks, human organs, and construction material.

1 Introduction

In the past decades, ERT as a cost-effective method has shown its advantages in many areas such as landfill management (Augusto et al., 2017; Dumont et al., 2018), thermal energy monitoring (Hermans et al., 2012; Lesparre et al., 2019), saltwater intrusion mapping (Franco et al., 2009; Kazakis et al., 2016), hydrology survey (Apostolopoulos, 2008; Coscia et al., 2012), etc. These applications all share the commonality that the observed objects are half-space conditions.

In recent decades, ERT has been applied to many other areas, which focus on cylindrical objects. For example, Thanh et al. (2006) proposed using ERT method for evaluating grouting performance after injection. Karhunen et al. (2010) applied ERT for three-dimensional imaging of concrete and their results including numerical modeling and experiments indicated that ERT might be a feasible modality for non-destructive evaluation of concrete. Sapkota et al. (2015) presented an application of ERT for the visualization of a thrombus in blood. Sardeshpande et al. (2016)

adopted ERT technique to obtain the mixture distribution across the cross-section of the mixing vessel. Ren et al. (2017) used ERT to measure the local velocity of shampoo in an in-line pipeline loop. Ren et al. (2019) investigated the influence of moisture content and water-cement ratio on resistivities of different kinds of cement specimens by ERT experiment and the results implied that ERT technique has potential in defect detection and in-situ monitoring in cement mortar. Losso et al. (2020) used ERT to study seasonal changes in tree trunks. Rao et al. (2021) used ERT to test, visualize, and evaluate the progress of crystallization processes.

The ERT method utilizes a pair of electrodes as transmitters to inject currents and another pair of electrodes as receivers to measure the responding voltages, which give a comprehensive discernment of the object. For cylindrical objects, we usually employ the point currents and reconstruct the resistivity of the cross-section (Bieker et al., 2010; Elliott et al., 2016; Guyot et al., 2013). Thus the source is three-dimensional but the object is two-dimensional. We call this the 2.5-dimensional ERT. With the increasing applications of ERT in cylindrical objects, the research corresponding to the 2.5-dimensional inversion algorithm is becoming more and more important.

There are mainly two kinds of inversion algorithms for the ERT of cylindrical objects, one of which is the absolute ERT represented by the Guasi-Newton algorithm (Loke and Barker, 1996). The absolute ERT usually consists of iterative processes and is theoretically applicable. However, this technique lacks robustness (Brazey et al., 2022). The other inversion algorithm is the differential ERT, which is a one-step linearized reconstruction algorithm represented by the maximum a posteriori approach (Adler and Guardo, 1996). It is more robust against modeling errors and can achieve fast (near real-time) image reconstruction. Therefore the differential ERT has been applied in many works of literature (Cao et al., 2020; Xu et al., 2011; Zhang et al., 2012).

The forward modeling is an essential step of any inversion algorithm (Gao et al., 2020; Günther et al., 2006). The commonly employed approaches for solving the Laplace equation in forward modeling include the finite-difference method (Tsili et al., 2000; Wu et al., 2003), boundary element method (Mukanova B 2018; Xu et al., 1998), finite element method (Ren Zhengrong 2010; Wu, 2003; Yang et al., 2017), etc. The finite element method has the advantage of high flexibility, making it suitable for modeling cylindrical objects. For the 2.5-dimensional ERT, the Fourier transform is employed to convert the three-dimensional cylindrical model into the two-dimensional cross-sectional circular model. And the inverse Fourier transform is then applied to convert the potential in the wavenumber domain to the potential in the spatial domain. The selection of the wavenumbers for the inverse Fourier transform is very important to improve the accuracy while reducing the calculation time (Xu et al., 2000). The optimization wavenumber selection (Xu et al., 2000) can achieve very high accuracy for the half-space condition. However, when referring to the forward modeling of a cylindrical model, its performance has not been developed yet. Most of the literature directly use the optimization wavenumbers that are calculated based on half-space condition. In this paper, we analyze the inapplicability of this kind of optimization wavenumbers on the 2.5-dimensional ERT of cylindrical objects and modify them for better modeling of cylindrical objects.

We firstly introduce briefly the basic theory of the 2.5-dimensional forward modeling of infinitely long cylindrical models using finite elements on unstructured grids. Secondly, we analyze the approximate analytic solution of the circumference potential distribution of an infinitely long homogeneous cylindrical model, based on which the corresponding modified optimization wavenumbers and the apparent resistivity tomography algorithm are proposed. Thirdly, by combing the modified optimization wavenumbers, we conduct the differential ERT of

a synthetic model. Lastly, an experiment is conducted to prove the accuracy of this 2.5-dimensional modified wavenumber selection based resistivity reconstruction method for cylindrical objects through comparisons.

2 Theory

2.1 The 2.5-dimensional Forward Modeling of Cylindrical Objects

The direct current potential obeys the Laplace equation (Rücker et al., 2006)

$$\nabla \cdot [\sigma(x,y,z)\nabla U(x,y,z)] = -I \cdot \delta(x-x_0) \cdot \delta(y-y_0) \cdot \delta(z-z_0) \quad (1)$$

where σ represents the conductivity, U represents the potential, and δ represents the Dirac function related to the point source. For an infinitely long cylinder extending along the *y*-axis with center (0,0,0), we conduct the Fourier transform to simplify the three-dimensional equation into 2.5-dimension by converting y into wavenumber λ and U into V. And the Neumann boundary condition is employed

$$\left.\frac{\partial U}{\partial \boldsymbol{n}}\right|_{\Gamma_1} = 0 \quad (2)$$

A mesh generator (Persson and Strang, 2004) is used to discretize the solution domain into unstructured triangular meshes, this grid type is flexible and allows for local refinement, thus can better simulate a round disk model and reduce the number of nodes. The finite element method (Coggon, 1971) is applied to solve the equation (1) as

$$\boldsymbol{K} \cdot \boldsymbol{V} = \boldsymbol{I} \quad (3)$$

where the system matrix $\boldsymbol{K}$ is sparse and symmetric, $\boldsymbol{V}$ is a vector consisting of the potentials in the wavenumber domain at all nodes and $\boldsymbol{I}$ is a vector representing the source distribution. After solving equation (3), we conduct the inverse Fourier transform to obtain the potential value

$$U(x,0,z) = \frac{2}{\pi}\int_0^{+\infty} V(x,\lambda,z) \cdot d\lambda \quad (4)$$

Because V is a series of discrete points and their values change with wavenumbers, which ranges from zero to infinity and their relationships are complex, the integral of V with respect to wavenumber λ can not be calculated directly. One approach to solve this problem is to approximate (4) as a sum gives

$$U(x,0,z) = \sum_{j=1}^{m} V(x,\lambda_j,z) \cdot g_j \quad (5)$$

where m is the total wavenumbers, λ_j is the discretized value of λ and g_j is the corresponding weighting coefficient selected by the optimization wavenumber selection method (Xu et al., 2000). This traditional optimization wavenumber selection method is frequently used in 2.5-dimensional forward modeling of the half-space because of its stability and high accuracy. During the wavenumber selection, the author employs V as $K_0(\lambda \cdot l)/(2\pi)$, where l is the distance between the current source and the calculated point and K_0 is the zero-order modified Bessel function of the second kind. It is the analytic solution of V when the model is a homogeneous half-space. However, when the object is a cylinder, the analytic solution of V is definitely different from those

of the half-space. Nevertheless, many researches applied the traditional optimization wavenumbers to calculate λ and g directlyfor the resistivity modeling of cylindrical objects, thus not fitted for cylindrical models and can cause great errors.

To prove this point of view, we introduce an infinitely long homogeneous cylindrical model, as is shown in figure 1, to analyze the relationship between V and λ, and compare its V to that of the half-space condition. The radius of the cylinder is 0.5m and the resistivity of the cylinder is 600Ω•m. The two current electrodes A and B are placed on (0.5, 0) and (-0.5, 0), and their current intensities are -0.02A and 0.02A respectively. θ_{AB} stands for the included angle between A and B. θ is the included angle between the current electrode A and the measurement point. 201 wavenumbers ranging from 0.00001 to 81 are employed.

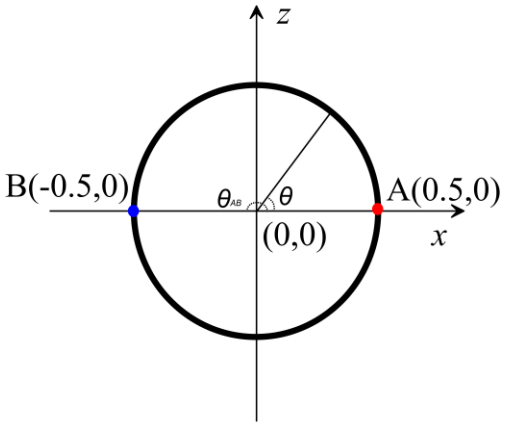

Figure 1. The cross section of the homogeneous cylindrical model.

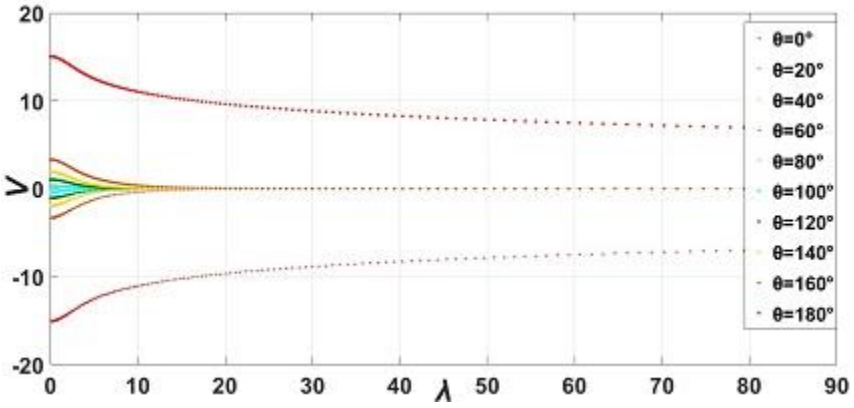

Figure 2. The relationship between V and wavenumber λ on different measurement points.

The calculated V changing with wavenumbers on different points of the circumference are shown in figure 2. For a particular point represented by θ, its potential U is the integral of $V(\lambda)$ multiply by $2/\pi$. When θ equals 0° and 180°, the functions $V(\lambda)$ are not convergent to zero, illustrating that the potentials in these two points are infinite. These curves correspond to the fact that the potentials in the point sources are infinite.

For a particular point, take θ equals 160° as an example. Figure 3 shows the difference of V between the cylindrical model and the half-space condition. The difference can influence the

wavenumber selection results and finally cause errors in forward modeling. To avoid this in the 2.5-dimensional simulation of the cylindrical model, the cross-section potential distribution should be analyzed in order to modify the optimization wavenumber selection.

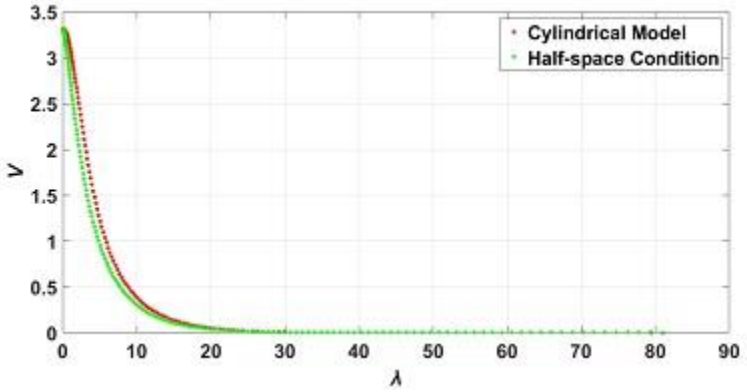

Figure 3. The difference of V between the cylindrical model and the half-space condition when θ equals 160°.

2.2 The Approximate Analytic Solution

Because the optimization wavenumber selection method is based on the analytical solution of the potential value, we must first analyze the analytic solution of the circumference potential distribution of an infinitely long homogeneous cylindrical model. During the numerical simulation, for a specific triangle mesh e

$$K_{rs}^{e} = \sigma_e \left[\frac{1}{2\Delta}(b_r b_s + c_r c_s) + \frac{\Delta \cdot \chi \cdot \lambda^2}{6}\right]; s,r=i,j,m; \chi = \begin{cases} 2 & (r = s) \\ 1 & (r \neq s) \end{cases} \quad (6)$$

where *i, j, m* are the numbers of mesh points, Δ is the area of the mesh, σ_e is the conductivity, and *b* and *c* stand for the coefficients related only to the location of the mesh. Since σ_e is proportional to $\boldsymbol{K}$ and $\boldsymbol{K}$ is inversely proportional to $\boldsymbol{V}$, it can be easily concluded that the conductivity is inversely proportional to $\boldsymbol{V}$, which means that the resistivity ρ is proportional to potential $U(\theta)$. Similarly, the current I is proportional to $U(\theta)$ because it is proportional to $\boldsymbol{V}$, and $\boldsymbol{V}$ is proportional to $U(\theta)$.

The relationship between radius R and circumferential potential $U(\theta)$ can not be directly seen from the formula. A hypothesis-verification method is used to confirm that R is inversely proportional to the circumferential potential $U(\theta)$.

In order to avoid the influence of wavenumber selection on the calculation of potential value, we employ the fitting formula to explicitly solve the inverse Fourier transform of the wavenumber domain and derive the approximate analytical potential solution on the cross-section where the point source is located. 201 wavenumbers are included in the fitting. Although the computing time is relatively longer, the accuracy can be much higher.

The circumference potentials of two homogenous cylindrical models (Model 1 and Model 2) are calculated. The radius of Model 1 is 0.5m and the resistivity of Model 1 is 600Ω•m. The two current electrodes are placed on (0.5, 0) and (-0.5, 0), and their current intensities are -0.02A and 0.02A respectively. The parameter setting of model 2 is the same as model 1 except that the radius is set to be 0.3m. With U_1 and U_2 being the circumferential potential of model 1 and model

2 respectively, as are shown in figure 4, the ratios between U_1 and U_2 are almost equal to 1.667 except for the points around 0°, 90°, 180°and 270°, where the potential equals either zero or infinite, making the ratio meaningless. Nevertheless, for the other points, the ratios stay quite stable at 1.667, which is precisely the same as the ratio between the radius of model 2 and model 1. To date, all the models we have calculated satisfy this rule. Therefore, we confirm that the radius R is inversely proportional to the circumferential potential $U(\theta)$ for an infinitely long homogeneous cylindrical model. This conclusion can be also seen in the paper of Weidelt and Weller (1997).

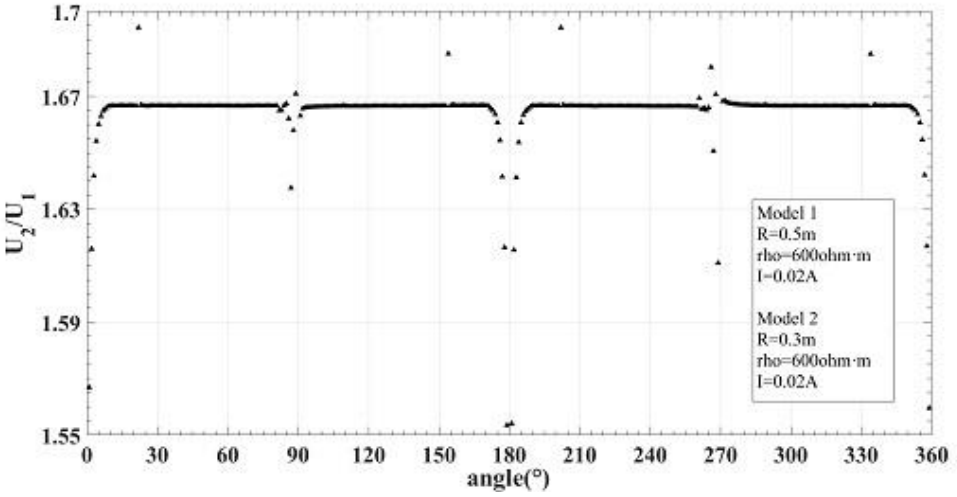

Figure 4. The ratio between U_2 and U_1.

From the above numerical analysis, we can conclude that $U = \frac{I\rho}{R} f_{\theta_{AB}}(\theta)$. $f_{\theta_{AB}}(\theta)$, which we define as source function, is a function of θ and its coefficients are determined only by θ_{AB}. For a specific homogeneous cylinder, when given a certain θ_{AB}, V of a certain λ can be numerically calculated, thus the V is the function of λ. Nevertheless, they are discrete nodes. To overcome the discrete integration problem, we use the following process to calculate $f_{\theta_{AB}}(\theta)$. First of all, fitting the $V(\lambda)$ with an elementary function. Secondly, applying function (4) to calculate the circumferential potential directly since the $V(\lambda)$ is an elementary function after fitting. For better understanding, the circumferential potential calculated by this fitting method is denoted by $U_{fit}(\theta)$. Lastly, combining the analyses above, $U_{fit}(\theta)$ equals to $\frac{I\rho}{R} f_{\theta_{AB}}(\theta)$. Then we acquire

$$f_{\theta_{AB}}(\theta) = \frac{R}{I \cdot \rho \cdot U_{fit}(\theta)} \tag{7}$$

It should be noted that for a certain θ_{AB}, the $f_{\theta_{AB}}(\theta)$ can be calculated and stored on a hard disk. Summarizing the results in the above sections we write the relationship between the circumferential potential of a cylindrical model and other parameters as

$$U(\theta) = \frac{I \cdot \rho}{R} f_{\theta_{AB}}(\theta) \tag{8}$$

We call the formulation (8) the approximate analytic solution of the circumferential potential distribution of an infinite homogeneous cylindrical model. This function can be used to modify the optimization wavenumber selection and calculate the geometric factor that are suitable for cylindrical objects.

2.3 The Modified Optimization Wavenumber Selection

Assume using *n* electrodes in the calculation, the included angle between current electrode A and these nodes are $\theta_1 \ldots \theta_i \ldots \theta_n$ and the corresponding coordinates are $(x_1, z_1) \ldots (x_i, z_i) \ldots (x_n, z_n)$. m denotes the quantity of the total used wavenumbers. Combining equation (5) and equation (8) we acquire

$$\frac{I \cdot \rho}{R} f_{\theta_{AB}}(\theta_i) = \sum_{j=1}^{m} V(x_i, \lambda_j, z_i) \cdot g_j \tag{9}$$

For an infinitely long homogeneous cylindrical model,

$$\sum_{j=1}^{m} V(x_i, \lambda_j, z_i) \cdot g_j \cdot R / [I \cdot \rho \cdot f_{\theta_{AB}}(\theta_i)] \approx 1 \tag{10}$$

The matrix form of equation (10) is

$$\boldsymbol{Ag} \approx \boldsymbol{L} \tag{11}$$

with the element of matrix $\boldsymbol{A}$ ($n \times m$ dimensions) being $a_{ij} = R \cdot V(x_i, \lambda_j, z_i)/[I \cdot \rho \cdot f_{\theta_{AB}}(\theta_i)]$, the element of matrix $\boldsymbol{g}$ ($m \times 1$ dimensions) being g_j and $\boldsymbol{L}$ being the $n \times 1$ dimensional unit vector. By incorporating the optimization wavenumber selection algorithm (Xu et al., 2000), the optimized wavenumbers and the corresponding weighting coefficients can be calculated iteratively.

It should be noted that both θ_{AB} and R could greatly influence the optimized wavenumber series. To avoid the influence of R, we propose a new way named as the converting process to avoid its influences basing on the fact that the radius R is inversely proportional to $U(\theta)$ for a cylindrical model. We only store the optimized wavenumber series when the radius equals a standard value R_0. When the radius of the model in the real case equals R_1, we first enlarge the discrete model linearly into cylinder R_0, apply the stored optimized wavenumber series to the forward modeling process and then multiply the potential by R_0/R_1.

2.4. The Differential ERT Algorithm

Typically, the differential ERT uses the data sets collected before and after the resistivity change to reconstruct the image. Set the model resistivity and the detected apparent resistivity distribution at time t_1 as $\boldsymbol{\rho}'$ and $\boldsymbol{\rho}_s'$ respectively. At time t_2, the resistivity and the detected apparent resistivity distribution change into $\boldsymbol{\rho}''$ and $\boldsymbol{\rho}_s''$ respectively. Let $\boldsymbol{x} = log_e \boldsymbol{\rho}'' - log_e \boldsymbol{\rho}'$ and $\boldsymbol{z} = log_e \boldsymbol{\rho}_s'' - log_e \boldsymbol{\rho}_s'$ (Adler and Guardo, 1996). For small changes around a background resistivity the relationship between x and z can be linearized as (Graham and Adler, 2006)

$$\boldsymbol{z} = \boldsymbol{Jx} + \boldsymbol{n} \tag{12}$$

where $\boldsymbol{J}$ is the Jacobian matrix (m×n dimensions, m: total measurements, n: total mesh grids) with its element $J_{ij} = \frac{\partial log \rho_{si}}{\partial log \rho_j}$ being $\frac{\partial log \rho_{si}}{\partial log \rho_j}$. ρ_{si} denotes the apparent resistivity during the *i-th* data collection and ρ_j denotes the model resistivity on the *j-th* mesh. $\boldsymbol{n}$ denotes the noise matrix. In order to overcome the ill-conditioning of $\boldsymbol{J}$ we solve (12) using the following regularized inverse (Graham and Adler, 2006):

$$\boldsymbol{x} = (\boldsymbol{J^T W J} + \beta \boldsymbol{R})^{-1} \boldsymbol{J^T W z} = \boldsymbol{Bz} \tag{13}$$

where $\boldsymbol{R}$ is a regularization matrix, β is a scalar hyperparameter (Batu and Çetin, 2008; Braun et al., 2017; Graham and Adler, 2006) that controls the amount of regularization and $\boldsymbol{W}$ is a $m \times m$ dimensional diagonal matrix with its diagonal element W_{ii} being $1/\eta_i^2$. η_i^2 is the noise variance of the *i-th* data collection. Usually there are three ways to calculate $\boldsymbol{R}$. (1) $\boldsymbol{R} = \boldsymbol{I}$, making equation (13) the *0-th* order Tikhonov algorithm. (2) $\boldsymbol{R} = diag(\boldsymbol{H^T H})$, making equation (13) the regularization matrix used in the NOSER algorithm (Cheney et al., 2010), (3) R is modeled as a spatially invariant Gaussian high pass filter (Adler and Guardo, 1996).

3. Experimental Experiments

3.1. The Apparent Resistivity Tomography for the Cylindrical Object

By employing the modified optimization wavenumbers in the 2.5-dimensional resistivity forward modeling, we can obtain the potential distribution of the cylinder cross-section. The process of converting the potential into apparent resistivity should also be adapted accordingly because this is also based on the analytic solution of the detected objects. The key to calculate the apparent resistivity is the geometric factor *G*. In analogy with the geometric factor calculation of half-space, we propose an algorithm to calculate the geometric factor of cylindrical models. Name the two receivers as M and N and the corresponding potentials of the cylinder model are U_{M} and U_{N} respectively. Then we acquire

$$U_{\mathrm{M}} = \frac{I \cdot \rho}{R} f_{\theta_{AB}}(\theta_{\mathrm{M}}) \tag{14}$$

$$U_{\mathrm{N}} = \frac{I \cdot \rho}{R} f_{\theta_{AB}}(\theta_{\mathrm{N}}) \tag{15}$$

where θ_{M} and θ_{N} stand for their locations on the circumferential surface. The potential difference between M and N is

$$\triangle U_{\mathrm{MN}} = \frac{I\rho}{R}\left[f_{\theta_{AB}}(\theta_{\mathrm{M}}) - f_{\theta_{AB}}(\theta_{\mathrm{N}})\right] \tag{16}$$

Rewrite equation (16) as

$$\rho = \frac{\triangle U_{MN} \cdot R}{I \cdot \left[f_{\theta_{AB}}(\theta_{\mathrm{M}}) - f_{\theta_{AB}}(\theta_{\mathrm{N}})\right]} \tag{17}$$

Then the geometric factor of the cylindrical model should be：

$$G = \frac{R}{f_{\theta_{AB}}(\theta_{\mathrm{M}}) - f_{\theta_{AB}}(\theta_{\mathrm{N}})} \tag{18}$$

Using the geometric factors introduced above, we conduct the forward modeling of three models using the Wenner and dipole-dipole array. Figure 5 shows these two kinds of electrode arrangements. C_1 and C_2 stand for the two current electrodes, P_1 and P_2 stand for the two receivers, *a* and *s* are the electrode spacing and number, *S* is the total detected layer and *t* is the total electrodes. For the Wenner array, the equally spaced C_1-P_1-P_2-C_2 moves one by one and detects *t* times in each layer. For dipole-dipole array, C_1-C_2 and P_1-P_2 remain as *a*, C_2-P_1 equals to $s \times a$ and still detect t times in each layer.

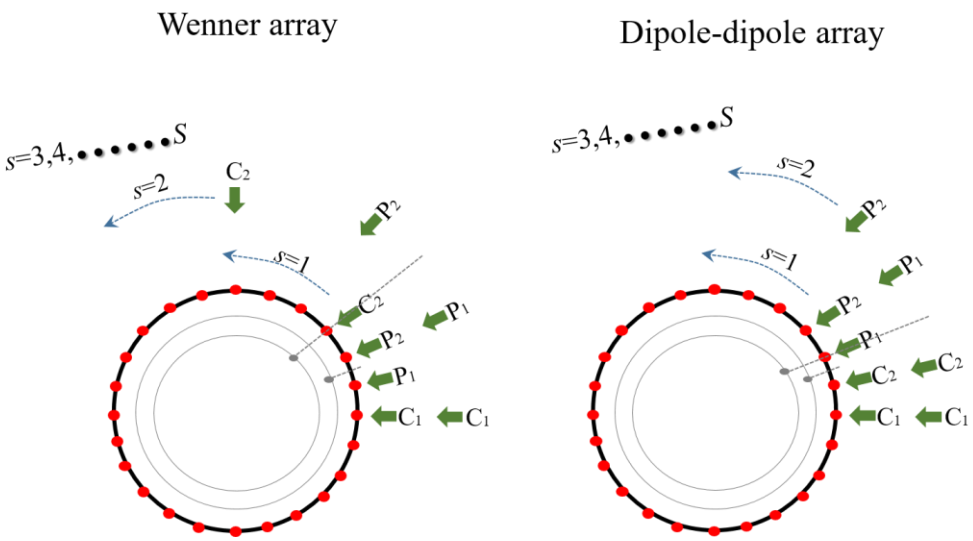

Figure 5. Wenner array and dipole-dipole array.

Figure 6 shows the calculated apparent resistivity results of three kinds of models. Thirty−two electrodes are employed and the radius is 0.2m. Compared with Wenner array, the dipole-dipole array has a higher contrast, which means that it is more sensitive to both anomaly and noise. When the anomaly locates in the central, the two apparent resistivity contour maps may be able to show its location, but when the anomalies locate otherwise or have a complex shape, the apparent resistivity distributions are not enough to recognize the anomaly. In some cases, the apparent resistivity distribution of the Wenner array is totally contrary to the results of dipole-dipole array because of the different location of the electrodes. The apparent resistivity can indeed reveal parts of the information in the cylindrical bodies, especially when there are no anomalies or the anomalies are located in the central. However, it is somehow limited for the analysis of complicated objects. For better application of ERT, more works need to be done to reconstruct the resistivity distribution.

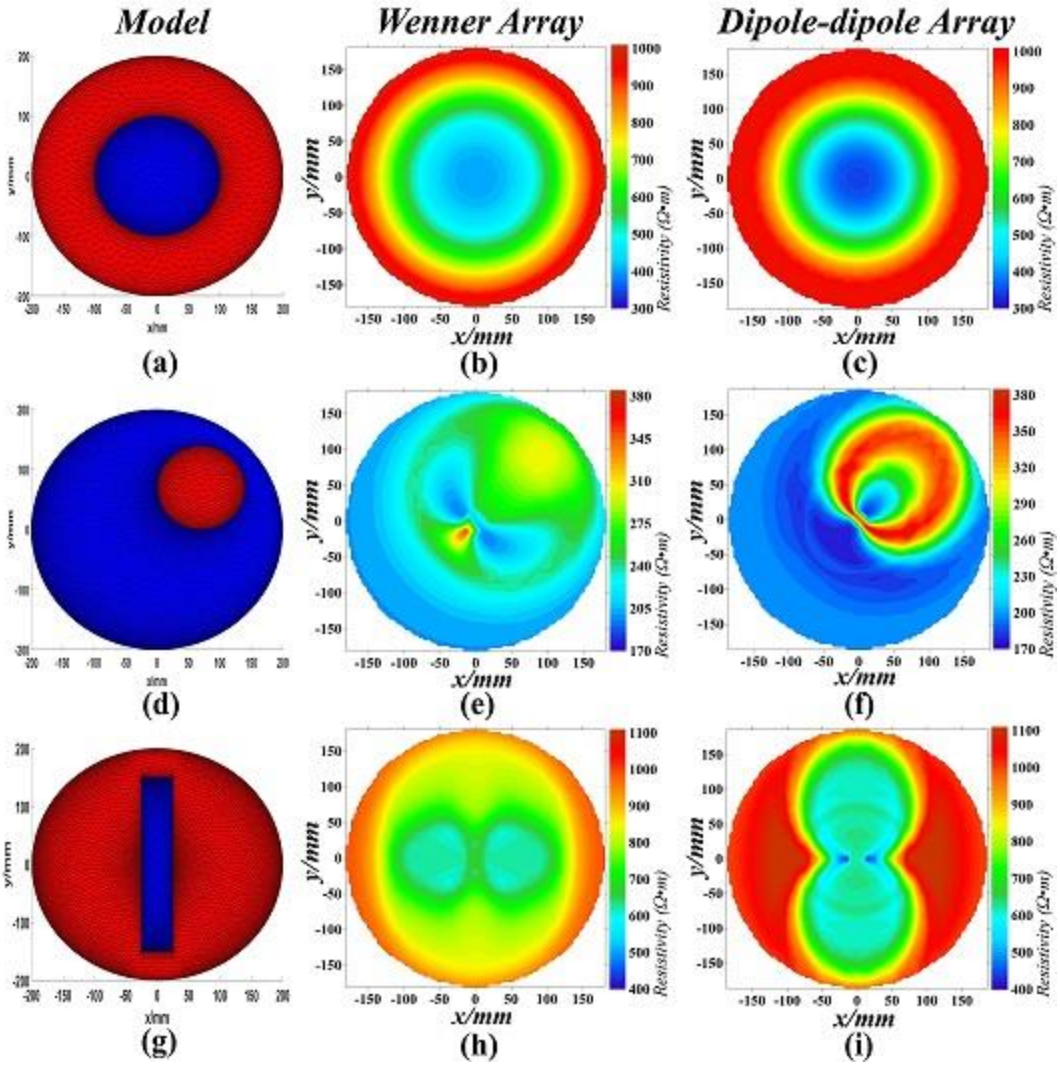

Figure 6. Apparent resistivity (Ω•m) calculation results of three different models. First column: (a), (d) and (g) are three different models with unstructured meshes, the red part is $1000\,\Omega\cdot m$ and the blue part is $200\,\Omega\cdot m$. Second column: (b), (e) and (h) are the apparent resistivity distributions of (a), (d) and (g) respectively using the Wenner array. Third column: (c), (f) and (i) are the apparent resistivity distributions of (a), (d) and (g) respectively using the dipole-dipole array.

3.2. The differential ERT of the synthetic data

We use the differential ERT mentioned in section 2.4 to retrieve the resistivity distribution of model 3 (Figure. 7) from the forward modeling result. As is shown in figure 7, model 3 is a cylinder with two anomalies located on edge, and its radius is 0.2m. The resistivities in the red, blue, and grey part are 1000Ω•m, 200Ω•m and 400Ω•m respectively. Twenty-four electrodes are employed. The total detected layers for the Wenner and dipole-dipole array are seven and twenty-one. During the inversion, $\eta_i^2 = 700$, $\boldsymbol{R} = diag(\boldsymbol{H}^T\boldsymbol{H})$ and β=0.016. The model detected in t_1 is set as a homogenous cylindrical model.

Figure 7 displays the parameters and unstructured meshes of model 3 in the first row. The second row introduces the Wenner array forward (left) and inversion (right) results and the third row

displays dipole-dipole array forward (left) and inversion (right) results. The reconstructed images of both the Wenner array and dipole-dipole array show high resolutions of the two adjacent anomalies and the inversion processes of both arrays only take about 3.67 seconds on a computer(Intel(R) Core(TM) i3-2100 CPU @ 3.10GHz RAM 16GB) since the Jacobian matrix can be calculated in advance and stored on the hard disk.

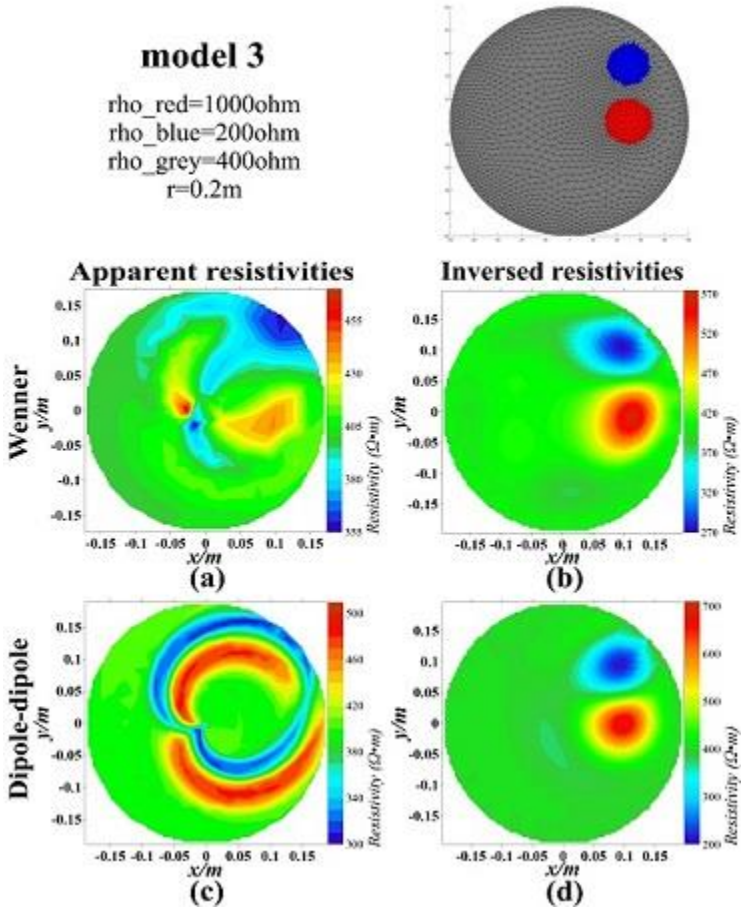

Figure 7. Apparent resistivity (Ω•m) distributions of model 3 and their inversed resistivity distributions. (a): Apparent resistivity distributions of model 3 using the Wenner array. (b): Inversed resistivity distributions of (a) using the differential ERT. (c) Apparent resistivity distributions of model 3 by the dipole-dipole array. (d) Inversed resistivity distributions of (c) by the differential ERT.

4. Experimental Results and Analysis

4.1. Experimental Set-up

For experimental model preparation, four steps are included. (1) Making the cylinder tube tank: Prepare a cylinder PVC tube of radius 99.75mm and height 1 m with the bottom glued with a plastic board. Punch equidistantly twenty-four holes of radius about 2mm on the circumference of height 0.5m. (2) Handcrafting the microelectrode: To decrease as much as possible the influence of the electrodes, we need to keep the radius as small as possible. Cut the multi-strand copper wire into 2cm long and peel off the rubber. Each copper thread can be used as a microelectrode. The

radius of our microelectrodes is less than 0.5mm. Inserting these microelectrodes into the holes of the tube one by one and seal the hole with glue. (3) Preparing the conductive water: Add 2.85g sodium chloride (NaCl) crystal to 30L distilled water. The average resistivity of this NaCl solution is 36.56Ω·m after several measurements. Pour the conductive water into the cylindrical tube model. (4) Simulating the anomaly: We put a homogenous rubber bar of radius 36.485mm and height 1.08m into the cylinder tank. Its average resistivity is estimated at 250 Ω·m after several detections.

After model preparation, we use the DUK-2B Multi-Electrode Resistivity Survey System (CGE (Chongqing) Geological Instrument Co., Ltd) for data collection and artificially transfer the electrode. Figure 8 shows the detections of the two models in the lab. Model 4 is a homogenous cylinder filled with NaCl solution and model 5 has a rubber bar as an anomaly standing in the center.

Figure 8. The detection process.

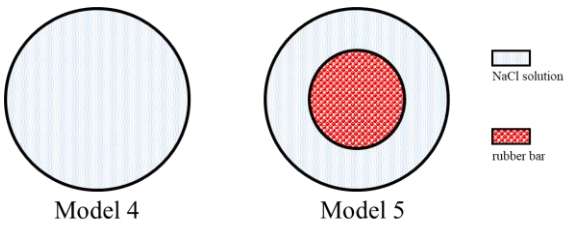

Figure 9. The cross sections of model 4 and model 5 in lab.

4.2. Experimental Results

To compare the accuracy of the forward modeling results using different kinds of wavenumbers, the resistance: *U/I* of both experimental results and numerical modeling results are calculated. For the numerical calculation, the other parameters are set the same with the laboratory model except for the wavenumbers in order to highlight its affection on accuracy. The difference between simulated resistance r_s and the experimental resistance r_e is calculated using $(r_s - r_e)/ r_e$. As is shown

in figure 10, the difference between the experimental resistance and the simulated resistance when using the traditional optimization wavenumbers ranges from -80% to -5%. The closer to the surface, the greater the difference can be. Nevertheless, when using the modified optimization wavenumbers, the difference ranges from 0% to 18% with few points reaching 34% randomly occurring because of the noise of the experimental data. Comparing the two kinds of simulated resistance data, we can easily draw the conclusion that the modified optimization wavenumbers can significantly reduce the error for 2.5-dimensional resistivity forward modeling of cylindrical objects. Although there are still some differences between the experimental data and the simulated data using the modified optimization wavenumbers, the simulation is not the only one to be responsible for that because the experimental data can be affected by many other factors. The fact that the modified optimization wavenumbers can achieve better 2.5-dimensional resistivity forward modeling results of cylindrical models is not a coincidence because this is also true for model 5. Figure 11 displays the simulated resistance distribution of both the Wenner and dipole-dipole array of model 5. The simulation results match pretty well with the experimental data.

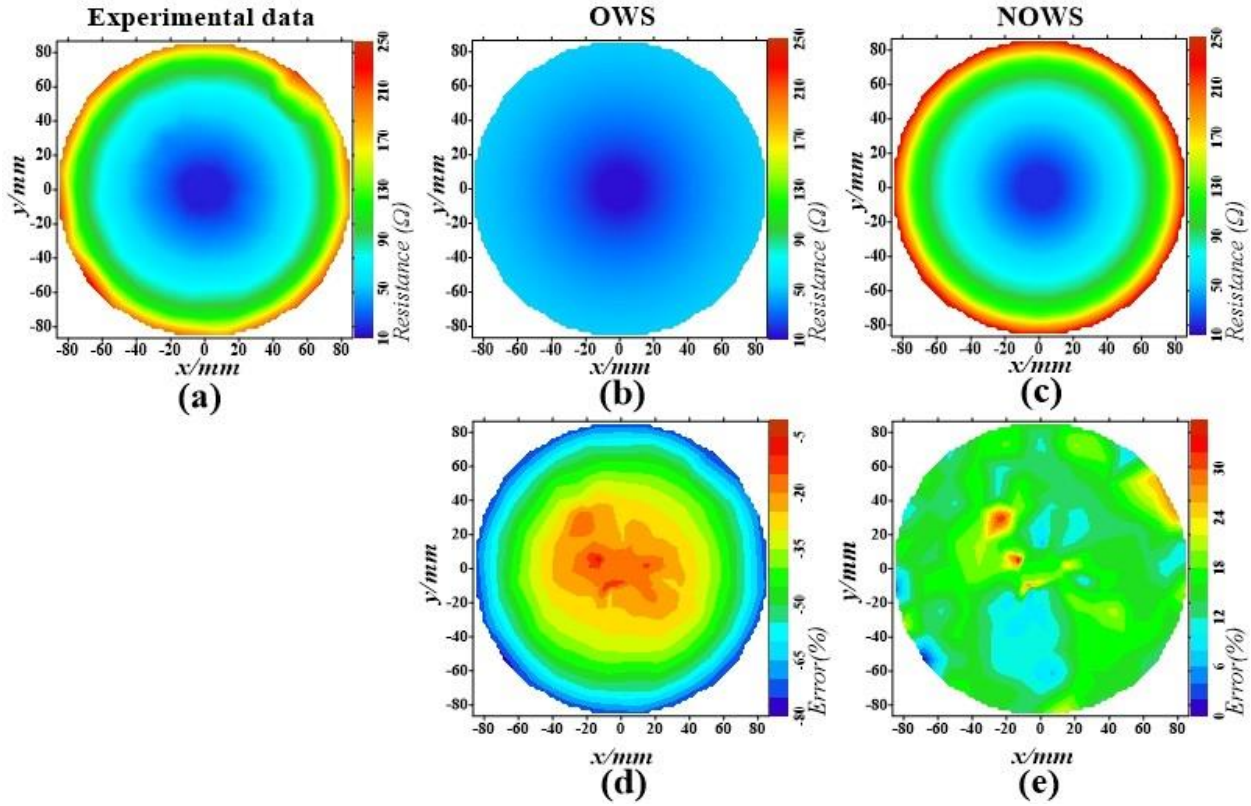

Figure 10. The experimental and simulated resistance (Ω) distribution of model 4 and their differences (%). (a) The experimental resistance distribution. (b) The simulated resistance distribution using the traditional optimization wavenumbers. (c) The simulated resistance distribution using the modified optimization wavenumbers. (d) The difference between the experimental resistance and the simulated resistance when using the traditional optimization wavenumbers. (e) The difference between the experimental resistance and the simulated resistance when using the modified optimization wavenumbers.

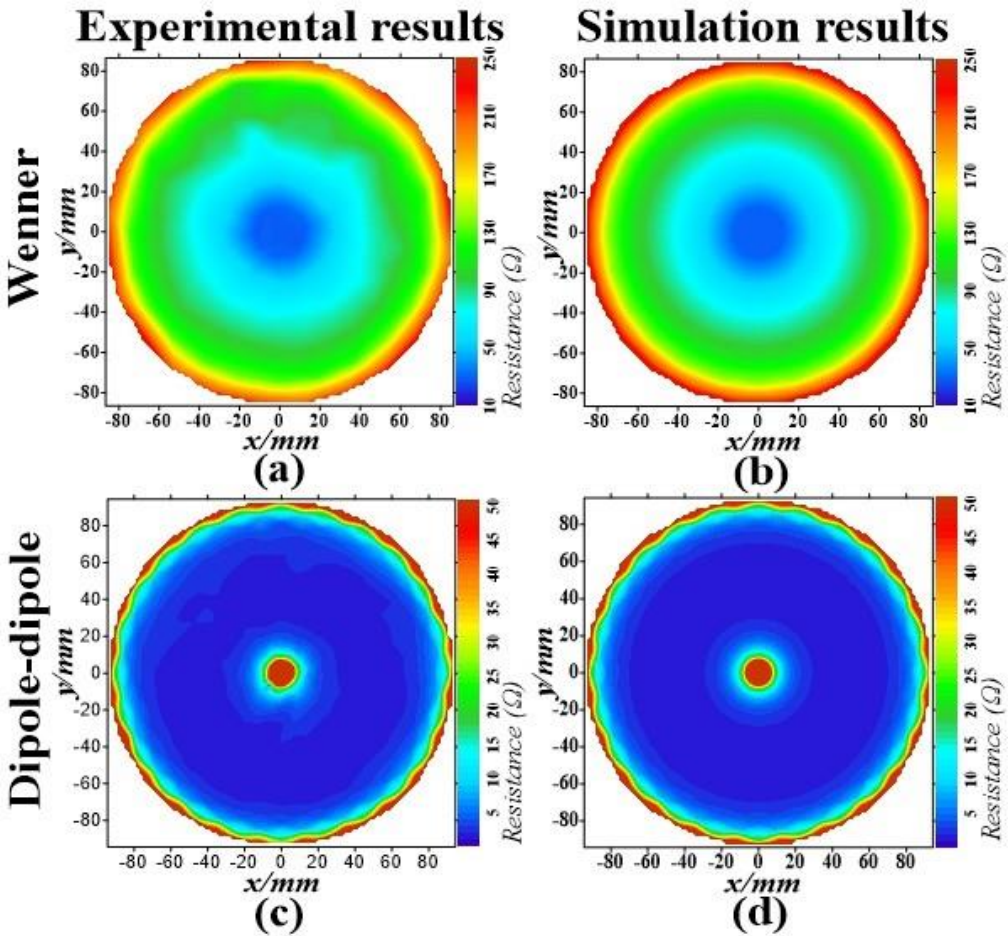

Figure 11. The experimental and simulated resistance (Ω) distribution of model 5. (a) The experimental resistance distribution using the Wenner array. (b) The simulated resistance distribution using the Wenner array. (c) The experimental resistance distribution using the dipole-dipole array. (d) The simulated resistance distribution using the dipole-dipole array.

To test the performance of the differential ERT method on the lab data, the experimental result of model 5 is employed in the calculation. During the image reconstruction, $\boldsymbol{R} = diag(\boldsymbol{H^T H})$, $\eta_i^2 = 700$ and β=0.016. The inversion results are shown in figure 12.

Though the inversion processes do not include the removal of bad points, the reconstructed images still match well with the real model. The inversions are done immediately since the Jacobian matrix is calculated and stored on a hard disk. This is to say that the differential ERT has the advantages of both time-saving and high anti-interference ability. When comparing the reconstructed images of the Wenner array and dipole-dipole array, we can see directly that the results of the dipole-dipole array have higher contrast. The total independent measuring points of the dipole-dipole array are more than those of the Wenner array, increasing its certainty greatly. Unlike in the half-space ground condition, the dipole-dipole array is less affected by electrode distance in cylindrical objects due to the relatively small detection area. The more independent measurements we take, the more accurate the inversion results will be. Therefore in the case of applying a certain number of electrodes, making as many independent measurements as possible in cylinder detection is an essential idea in designing electrode arrangements.

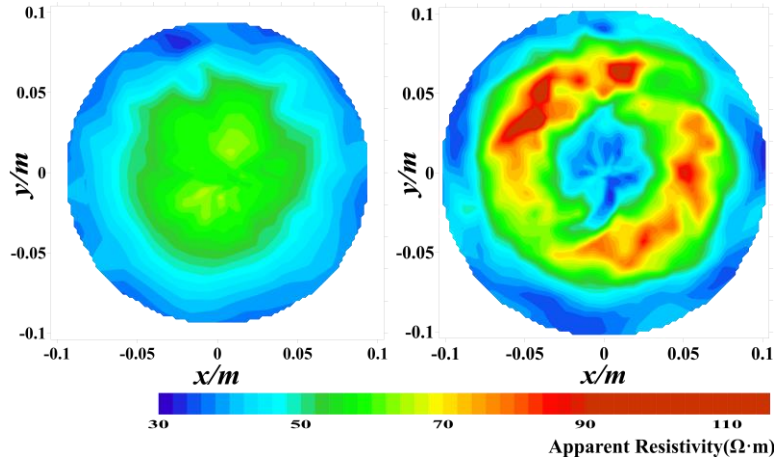

(a)

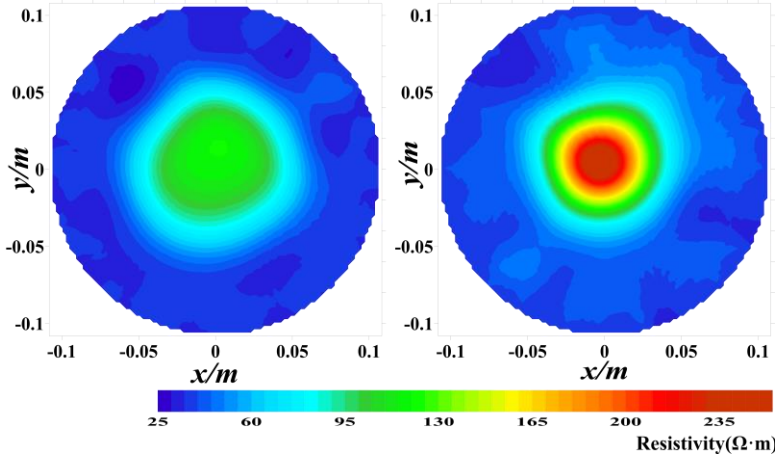

(b)

Figure 12. Inversion results of model 5 by the differential ERT. (a) The experimental apparent resistivity distribution by the Wenner array (left) and the Inversed resistivity distribution (right). (b) The experimental apparent resistivity distribution by the dipole-dipole array (left) and the inversed resistivity distribution (right).

5. Discussions

For decades, massive researches have proved that the ERT method performs pretty well in identifying low-resistivity (or high-resistivity) anomalies in the shallow half-surface. The numerical modeling and inversion algorithm together with the experiment described in this paper illustrate that the ERT can also be well applied to determine contrast resistivity anomalies of a cylindrical object. Thus enabling the ERT method to be applied to more areas such as tree trunk imaging for environmental protection, defect detection in construction materials, lung imaging for medical science, etc. However, there are several issues that still need to be addressed: the selection of hyperparameter in time difference imaging, the array arrangements, etc. Our next interest, for numerical imaging, is to study the high order differential ERT, and for in situ application is to propose a more suitable array arrangement and finally lead to better applications.

For the inversion part, the hyperparameter in this paper is chosen as 0.016 directly from an empirical point of view. Graham and Adler (2006) introduced five ways to objectively select hyperparameters. But for specific survey issues, the corresponding hyperparameter selection may need more specific discussions. The inversion results of model 3 in figure 7 show high resolutions of the two adjacent anomalies, however, two problems still remain. Firstly, their true resistivities are not revealed well. That's because the differential ERT method we use is a one-order linearized approximation. To achieve both high resolutions and true resistivity reconstructions, the high order image construction (Chan et al., 2000; Jiang et al., 2014) is suggested to be carefully studied and introduced into the geophysical inversion. Secondly, there are regular noises near the electrodes in the inversion results. These are also regular in other papers (D. Bieker et al., 2010; Bieker and Rust, 2010; Wang et al., 2016), we think that the main cause is that the potential around the current nodes are complicated and can't be perfectly matched with the fitted values. There are mainly two kinds of ways to solve this problem. One is to increase the accuracy of the approximate analytic solution of the infinitely long homogeneous cylindrical model and the other is to place the receivers far from the current nodes.

Vauhkonen et al. (1999) described that it is yet not clear to which task one should direct the effort, for example, the increase of the number of electrodes, estimation of feasible conditions for the termination boundary or the accuracy of the geometrical modeling of the object boundary. Well, in this paper we might have the answer. First, theoretically, the increasing number of electrodes does increase the accuracy of image reconstruction since it brings more information. Nevertheless, the number of electrodes we use should depend on the detection precision required. Second, the geometrical modeling of the object boundary does have a great influence on the forward modeling results. In our numerical analysis, the effect of boundary geometry is transferred into the effect of wavenumber selections on the forward modeling results. The error caused by wrongly selected wavenumbers, or wrongly described boundary geometry, can reach as many as 80%. Therefore, both the number of electrodes and the boundary conditions should be studied seriously.

6. Conclusions

For an infinitely long homogeneous cylindrical model, we summarize its circumferential potential distribution as $U(\theta) = \frac{I \cdot \rho}{R} f_{\theta_{AB}}(\theta)$. Thus the circumferential potential $U(\theta)$ is inversely proportional to the radius R and proportional to the current intensity I, the resistivity ρ and the source function $f_{\theta_{AB}}(\theta)$. $f_{\theta_{AB}}(\theta)$ is a function of θ and its coefficients are determined only by the included angle between two current electrodes. This relationship is easy but very significant because it is the basis of many other numerical approximations and no other papers have proposed this as far as we know. Basing on this newly proposed approximate analytic solution for the infinitely long homogeneous cylindrical model, the modified optimization wavenumber selection is derived, which is used for selecting wavenumbers for 2.5-dimensional resistivity modeling of cylindrical objects. The core idea of this adaption is to replace the analytic solutions of half-space ground with the approximate analytic solution of the infinitely long homogeneous cylindrical model. Both numerical results and experimental results have proved that it can greatly improve the accuracy of 2.5-dimensional forward modeling of cylinder objects.

In order to erase the effect of radius on wavenumber selection, which means preventing from selecting the optimized wavenumbers every time, we need to include the converting process in the computing process. The concept is to model the cylinder in a unified radius firstly and then convert the potential to the actual value basing on the fact that the potential is inversely proportional to the

448 radius. The apparent resistivity of cylindrical models can be pretty different due to their special
449 geometry. Basing on the approximate analytic solution for the infinitely long homogeneous
450 cylindrical model, we presented the geometric factor calculation method for apparent resistivity
451 tomography of cylindrical objects in analogy with the geometric factor calculation of half-space.

452 By incorporating all these new concepts in numerical simulation, we present the resistivity
453 reconstruction method for cylindrical objects. It is timesaving, cost-effective and has good anti-
454 interference capacity. The experimental results correlate pretty well with the numerical modeling
455 results, furtherly verifying that the modified optimization wavenumbers can result in better
456 accuracy than the traditional optimization wavenumbers and the proposed 2.5-dimensional fast
457 resistivity reconstruction scheme has great promise for cylindrical object imaging.

458 **Acknowledgments**

459 This work was supported in part by the Project of the State Key Research and Development Plan

460 under Grant No. 2018YFE0208300, in part by the National Natural Science Foundation of China

461 under Grant No. 41874084, U2039206, and in part by the Anhui Natural Science Foundation

462 under Grant 2008085QD176.

463 **References**

464 Adler A. & Guardo R., 1996 Electrical impedance tomography: regularized imaging and contrast detection.
465 *IEEE Transactions on Medical Imaging, 15*(2), 170-179. https://doi.org/10.1109/42.491418
466 Apostolopoulos G., 2008. Combined Schlumberger and dipole-dipole array for hydrogeologic
467 applications. *Geophysics, 73*(5), F189-F195. https://doi.org/10.1190/1.2950032
468 Augusto M. C., Innocenti H. L. P., Paulo N. & Melo I. L., 2017. Analysis of leaks from
469 geomembrane in a sanitary landfill through models of electrical resistivity tomography in
470 South Brazil. *Environmental Earth Sciences, 77*(1), 7. https://doi.org/10.1007/s12665-017-
471 7180-x
472 Batu Ö. & Çetin M., 2008. Hyper-parameter selection in non-quadratic regularization-based radar
473 image formation. *Proceedings of SPIE - The International Society for Optical Engineering,*
474 *6970*. https://doi.org/10.1117/12.782341
475 Bieker, Dirk, Rust & Steffen, 2010. Electric resistivity tomography shows radial variation of
476 electrolytes in Quercus robur. *Canadian Journal of Forest Research*. 40,1189-1193.
477 https://doi.org/10.1139/X10-076
478 Bieker D., Kehr R., Weber G. & Rust S., 2010. Non-destructive monitoring of early stages of white
479 rot by Trametes versicolor in Fraxinus excelsior. *Annals of Forest Science, 67*(2), 210-210.
480 https://doi.org/10.1051/forest/2009103
481 Bieker D. & Rust S., 2010. Non-destructive estimation of sapwood and heartwood width in Scots
482 pine (Pinus sylvestris L.). *Silva Fennica, 44*(2), 267-273. https://doi.org/10.14214/sf.153
483 Braun F., Proenca M., Sola J., Thiran J.-P. & Adler A., 2017. A Versatile Noise Performance
484 Metric for Electrical Impedance Tomography Algorithms. *IEEE Transactions on*
485 *Biomedical Engineering, 64*(10), 2321-2330. https://doi.org/10.1109/tbme.2017.2659540

Brazey B., Haddab Y. & Zemiti N., 2022. Robust imaging using electrical impedance tomography: review of current tools. *Proceedings of the Royal Society a-Mathematical Physical and Engineering Sciences, 478*(2258). https://doi.org/10.1098/rspa.2021.0713

Cao L., Li H., Fu D., Liu X. & Fu F., 2020. Real-time imaging of infarction deterioration after ischemic stroke in rats using electrical impedance tomography. *Physiological Measurement, 41*(1), 015004. https://doi.org/10.1088/1361-6579/ab69ba

Chan T., Marquina A. & Mulet P., 2000. High-Order Total Variation-Based Image Restoration. *SIAM Journal on Scientific Computing, 22*(2), 503-516. https://doi.org/10.1137/s1064827598344169

Cheney M., Isaacson D., Newell J. C., simske S. & Goble J., 2010. NOSER: An algorithm for solving the inverse conductivity problem. *International Journal of Imaging Systems & Technology, 2*(2), 66-75. https://doi.org/10.1002/ima.1850020203

Coggon J. H., 1971. Electromagnetic and Electrical Modeling by the Finite Element Method. *Geophysics, 36*(1), 132-155. https://doi.org/10.1190/1.1440151

Coscia I., Linde N., Greenhalgh S., Vogt T. & Green A., 2012. Estimating traveltimes and groundwater flow patterns using 3D time-lapse crosshole ERT imaging of electrical resistivity fluctuations induced by infiltrating river water. *Geophysics, 77*(4), E239-E250. https://doi.org/10.1190/Geo2011-0328.1

Dumont G., Robert T. & Nguyen F., 2018. Electrical resistivity tomography and distributed temperature sensing monitoring to assess the efficiency of horizontal recirculation drains on retrofit bioreactor landfills. *Geophysics, 83*(2), B13-B23. https://doi.org/10.1190/Geo2016-0622.1

Elliott M. L., Broschat T. K. & Göcke L., 2016. Preliminary Evaluation of Electrical Resistance Tomography for Imaging Palm Trunks. *Arboriculture & Urban Forestry, 42*(2), 111-119. https://doi.org/10.48044/jauf.2016.010

Franco R. d., Biella G., Tosi L., Teatini P., Lozej A., Chiozzotto B., . . . Gasparetto-Stori G., 2009. Monitoring the saltwater intrusion by time lapse electrical resistivity tomography: The Chioggia test site (Venice Lagoon, Italy). *Journal of Applied Geophysics, 69*(3-4), 117-130. https://doi.org/10.1016/j.jappgeo.2009.08.004

Gao J., Smirnov M., Smirnova M. & Egbert G., 2020. 3-D DC Resistivity Forward Modeling Using the Multi-resolution Grid. *Pure and Applied Geophysics, 177*(4), 1-17. https://doi.org/10.1007/s00024-019-02365-3

Graham B. M. & Adler A., 2006. Objective selection of hyperparameter for EIT. *Physiol Meas, 27*(5), S65-79. https://doi.org/10.1088/0967-3334/27/5/S06

Günther T., Rücker C. & Spitzer K., 2006. Three-dimensional modelling and inversion of DC resistivity data incorporating topography – II. Inversion. *Geophysical Journal of the Royal Astronomical Society, 166*(2), 506-517. https://doi.org/ 10.1111/j.1365-246X.2006.03011.x

Guyot A., Ostergaard K. T., Lenkopane M., Fan J. & Lockington D. A., 2013. Using electrical resistivity tomography to differentiate sapwood from heartwood: application to conifers. *Tree Physiology, 33*(2), 187-194. https://doi.org/10.1093/treephys/tps128

Hermans T., Vandenbohede A., Lebbe L. & Nguyen F., 2012. A shallow geothermal experiment in a sandy aquifer monitored using electric resistivity tomography. *Geophysics, 77*(1), B11-B21. https://doi.org/10.1190/geo2011-0199.1

Jiang L., Huang J., Lv X.-G. & Liu J., 2014. High-Order Total Variation-Based Image Restoration with Spatially Adapted Parameter Selection. *Proceedings of International Conference on*

Computer Science and Information Technology (Csait 2013), 255, 67-74. https://doi.org/10.1007/978-81-322-1759-6_9

Karhunen K., Seppänen A., Lehikoinen A., Monteiro P. J. M. & Kaipio J. P., 2010. Electrical Resistance Tomography imaging of concrete. *Cement and Concrete Research, 40*(1), 137-145. https://doi.org/10.1016/j.cemconres.2009.08.023

Kazakis N., Pavlou A., Vargemezis G., Voudouris K. S., Soulios G., Pliakas F. & Tsokas G., 2016. Seawater intrusion mapping using electrical resistivity tomography and hydrochemical data. An application in the coastal area of eastern Thermaikos Gulf, Greece. *Sci Total Environ, 543*(Pt A), 373-387. https://doi.org/10.1016/j.scitotenv.2015.11.041

Lesparre N., Robert T., Nguyen F., Boyle A. & Hermans T., 2019. 4D electrical resistivity tomography (ERT) for aquifer thermal energy storage monitoring. *Geothermics, 77*, 368-382. https://doi.org/10.1016/j.geothermics.2018.10.011

Loke M. H. & Barker R. D., 1996. Rapid least‐squares inversion of apparent resistivity pseudosections by a quasi‐Newton method. *Geophysical Prospecting, 44*(1), 131-152. https://doi.org/ 10.1111/j.1365-2478.1996.tb00142.x

Losso A., Sailer J., Br A., Ganthaler A. & Mayr S., 2020. Insights into trunks of Pinus cembra L.: analyses of hydraulics via electrical resistivity tomography. *Trees*. https://doi.org/ 10.1007/s00468-020-01976-x

Mukanova B M. I., 2018. The Boundary Element Method in the Sounding of Media with Ground Surface Relief. 115-152. https://doi.org/10.1007/978-3-319-72908-4

Persson P.-O. & Strang G., 2004. A Simple Mesh Generator in Matlab. *SIAM Review, 46*(2), 329-345. https://doi.org/10.2307/20453511

Rao G. R., Sattar M. A., Wajman R. & Jackowska-Strumillo L., 2021. Quantitative Evaluations with 2d Electrical Resistance Tomography in the Low-Conductivity Solutions Using 3d-Printed Phantoms and Sucrose Crystal Agglomerate Assessments. *Sensors, 21*(2), 1-31. https://doi.org/10.3390/s21020564

Ren H., Tian K., Hong S., Dong B., Xing F. & Qin L., 2019. Visualized investigation of defect in cementitious materials with electrical resistance tomography. *Construction and Building Materials, 196*(2019), 428-436. https://doi.org/10.1016/j.conbuildmat.2018.11.129

Ren Z., Kowalski A. & Rodgers T. L., 2017. Measuring inline velocity profile of shampoo by electrical resistance tomography (ERT). *Flow Measurement and Instrumentation, 58*(2017), 31-37. https://doi.org/10.1016/j.flowmeasinst.2017.09.013

Ren Zhengrong T. J., 2010. 3D direct current resistivity modeling with unstructured mesh by adaptive finite-element method. *Geophysics, 75*(1), H7. https://doi.org/10.1190/1.3298690

Rücker C., Günther T. & Spitzer K., 2006. Three-dimensional modelling and inversion of DC resistivity data incorporating topography I: Modelling. *Geophysical Journal International, 166*(2), 495-505. https://doi.org/ 10.1111/j.1365-246X.2006.03010.x

Sapkota A., Fuse T., Seki M., Maruyama O., Sugawara M. & Takei M., 2015. Application of electrical resistance tomography for thrombus visualization in blood. *Flow Measurement and Instrumentation, 46*(2015), 334-340. https://doi.org/10.1016/j.flowmeasinst.2015.06.023

Sardeshpande M. V., Kumar G., Aditya T. & Ranade V. V., 2016. Mixing studies in unbaffled stirred tank reactor using electrical resistance tomography. *Flow Measurement and Instrumentation, 47*(2016), 110-121. https://doi.org/10.1016/j.flowmeasinst.2016.01.003

Thanh N. D., Cho G. C., Sim Y. J. & Lee S. W., 2006. Evaluation of Grouting Performance Using Electrical Resistivity Tomography. *Key Engineering Materials, 321-323*, 1407-1410. https://doi.org/10.4028/www.scientific.net/KEM.321-323.1407

Tsili W., Sheng F. & Mezzatesta A. G., 2000. Three-dimensional finite-difference resistivity modeling using an upgridding method. *IEEE Transactions on Geoscience and Remote Sensing, 38*(4), 1544-1550. https://doi.org/10.1109/36.851954

Vauhkonen P. J., Vauhkonen M., Savolainen T. & Kaipio J. P., 1999. Three-dimensional electrical impedance tomography based on the complete electrode model. *IEEE Transactions on Biomedical Engineering, 46*(9), 1150-1160. https://doi.org/10.1109/10.784147

Wang H., Guan H., Guyot A., Simmons C. T. & Lockington D. A., 2016. Quantifying sapwood width for three Australian native species using electrical resistivity tomography. *Ecohydrology, 9*(1), 83-92. https://doi.org/10.1002/eco.1612

Weidelt P. & Weller A., 1997. Computation of geoelctrical configuration factor for cylindrical core samples. *Scientific Drilling, 6*(1), 27-34. https://doi.org/

Wu X., 2003. A 3-D finite-element algorithm for DC resistivity modelling using the shifted incomplete Cholesky conjugate gradient method. *Geophysical Journal International, 154*(3), 947-956. https://doi.org/10.1046/j.1365-246X.2003.02018.x

Wu X., Xiao Y., Qi C. & Wang T., 2003. Computations of secondary potential for 3D DC resistivity modelling using an incomplete Choleski conjugate-gradient method. *Geophysical Prospecting, 51*(6), 567-577. https://doi.org/10.1046/j.1365-2478.2003.00392.x

Xu C., Dai M., You F., Shi X., Fu F., Liu R. & Dong X., 2011. An optimized strategy for real-time hemorrhage monitoring with electrical impedance tomography. *Physiological Measurement, 32*(5), 585-598.

Xu S.-z., Duan B.-c. & Zhang D.-h., 2000. Selection of the wavenumbers k using an optimization method for the inverse Fourier transform in 2.5D electrical modelling. *Geophysical Prospecting, 48*(5), 789-796. https://doi.org/10.1046/j.1365-2478.2000.00210.x

Xu S., Zhao S. & Ni Y., 1998. A boundary element method for 2-D dc resistivity modeling with a point current source. *Geophysics, 63*(2), 399-404. https://doi.org/doi10.1190/1.1444339

Yang J., Liu Y. & Wu X., 2017. 3-D DC resistivity modelling with arbitrary long electrode sources using finite element method on unstructured grids. *Geophysical Journal International, 211*(2), 1162-1176. https://doi.org/10.1093/gji/ggx356

Zhang S., Xu G., Zhang X., Bo Z., Wang H., Xu Y., . . . Yan W., 2012. Computation of a 3-D Model for Lung Imaging With Electrical Impedance Tomography. *IEEE Transactions on Magnetics, 48*(2), 651-654. https://doi.org/10.1109/TMAG.2011.2174779